

Dynamic Stall Investigation on a Rotating semi-elastic Double-swept Rotor Blade at the Rotor Test Facility Göttingen

Martin Müller

Research Scientist

German Aerospace Center

Institute of Aeroelasticity

Göttingen, Germany

Armin Weiss

Research Scientist

German Aerospace Center

Institut of Aerodynamics and Flow Technology

Cologne, Germany

Johannes Niklas Braukmann

Research Scientist

Institut of Aerodynamics and Flow Technology

Göttingen, Germany

ABSTRACT

Experimental investigations of three-dimensional dynamic stall on a four-bladed Mach-scaled semi-elastic rotor with an innovative double-swept rotor blade planform are presented. The study focuses on the coupling between the aeroelastic behavior of the blade and the underlying aerodynamics. Blade bending moment and flap displacement measurements were conducted using strain gauges and optical tracking of blade tip markers. The aerodynamic behavior was characterized by means of unsteady surface pressure measurements using unsteady pressure-sensitive paint (iPSP) across the outer 65 % of the blade span and fast response pressure transducers at discrete locations. Different cyclic-pitch settings were investigated at a rotation frequency of $f_{\text{rotor}} = 23.6$ Hz, that corresponds to blade tip Mach and Reynolds numbers of $M_{\text{tip}} = 0.282 - 0.285$ and $Re_{\text{tip}} = 5.84 - 5.95 \times 10^5$. The findings reveal a detailed insight into the non-linear behavior in the flap movement during downstroke. iPSP and pressure transducer data indicates that this non-linear flap behavior is caused by a radially phase-shifted dynamic stall process at the forward and backward swept part of the blade.

NOTATION

a	Speed of sound (m/s)
b	Width of wind tunnel nozzle (m)
c	Blade chord length ($c_{\text{root}} = 0.072$ m)
C_p	Pressure coefficient
$C_p M^2$	Radial pressure coefficient
d	Marker distance (mm)
f	Frequency (Hz)
h	Height of wind tunnel nozzle (m)
M	Mach number
p	Pressure (Pa)
R	Rotor blade radius ($R = 0.65$ m)
Re	Reynolds number
r	Radial distance (m)
t	Time (s)
u	Rotation speed (m/s)
v	Flow velocity (m/s)
x	Chordwise distance from leading edge (m)
Θ	Blade pitch angle ($^\circ$)
Ω	Angular frequency
ρ	Air density (kg/m^3)
τ_{BT}	Blade tip camera exposure time (μs)

Subscripts

tip	Blade tip
root	Root of the blade
rotor	Relate to rotor
∞	Axial inflow
\uparrow	During upstroke motion
\downarrow	During downstroke motion
$\hat{\Theta}$	Cyclic-pitch amplitude
$\bar{\Theta}_{\text{root}}$	Collective-pitch angle

INTRODUCTION

A key limitation of the helicopter flight envelope is the dynamic stall phenomenon which causes noise and design-critical fluctuations of the associated lift, drag and pitching moment (Refs. 1, 2). Dynamic stall occurs on the retreating side of the rotor disk during forward and maneuver flight. Considering innovative blade geometries in the design phase of a helicopter rotor bears a great potential to improve these limitations. In order to understand the influence of alternative blade geometries, the interaction of the resulting aerodynamics, aeroelasticity and structural behavior need to be carefully studied.

Previous 2D and 2.5D aeroelastic experiments in the Transonic Wind Tunnel Göttingen (TWG) exhibited the complex-

ity of these kind of experiments, where combined measurements of model deformation, integral blade bending moment and surface pressure distribution were conducted (Refs. 3–8). In addition, numerical (Refs. 9, 10) and experimental (Refs. 11, 12) studies show the aerodynamic complexity of the dynamic stall phenomenon. According to the current state of research, the mechanism in 2D is extensively researched and well understood (Ref. 13). In 3D, a significantly increased complexity from an aerodynamic point of view has been shown (Ref. 14). In particular, radial effects are added during the transfer into a rotating system (Ref. 15). From experimental investigations on helicopter rotors it is known that the aerodynamic (Refs. 16, 17) and aeroelastic (Ref. 18) behavior of rotor blades with respect to stability, dynamic stall (Ref. 19) or flutter can only be determined by a combination of different measurement techniques.

The Rotor Test Facility Göttingen (RTG) at the German Aerospace Center (DLR) was designed for dynamic stall experiments in a rotating system with up to four rotor blades (Ref. 20). The phenomenon was studied using conventional rotor blades with a parabolic tip, both numerically (Refs. 21, 22) and experimentally (Refs. 23, 24), using local pressure transducers, tufts and Particle Image Velocimetry (PIV) measurements of the near wake. In a next step, an innovative double-swept rotor blade model for dynamic stall investigations at the RTG was developed and built at the DLR-Institute of Aeroelasticity (AE) (Ref. 25). First numerical investigations on the double-swept rotor blade indicated a different stall behavior when compared to a conventional planform (Ref. 26).

Moreover, unsteady surface pressure measurements by means of pressure-sensitive paint (iPSP) revealed first insights into the global pressure footprint of the innovative blade geometry while undergoing dynamic stall showing excellent agreement to numerical computations (Ref. 27). The focus of all previous dynamic stall investigations at the RTG was mainly with respect to rotor aerodynamics.

In the current study, the innovative double-swept rotor blade geometry was tested at the RTG under dynamic stall conditions using combined measurements of the aeroelastic and aerodynamic behavior. The flap displacement, the integral blade bending moment and the surface pressures were measured simultaneously. Selected iPSP results were presented previously in Ref. 27 with a focus on a comparison to numerical simulations. In this study, different iPSP results are shown and presented the context of aeroelastic measurements. Surface pressures were additionally recorded using fast response pressure transducers. Strain gauges were used to measure the integral blade bending moment as well as the flap displacement. The latter was also measured optically by tracking retro-reflective markers on the blade tip.

EXPERIMENTAL SETUP AND MEASUREMENT TECHNIQUES

Wind tunnel setup

The experiment was carried out at the RTG. An image of the experimental setup is depicted in Fig. 1. The vertical rotor plane was situated 2.3 m in front of the nozzle of the Eiffel type wind tunnel. The nozzle had a cross section of 1.6

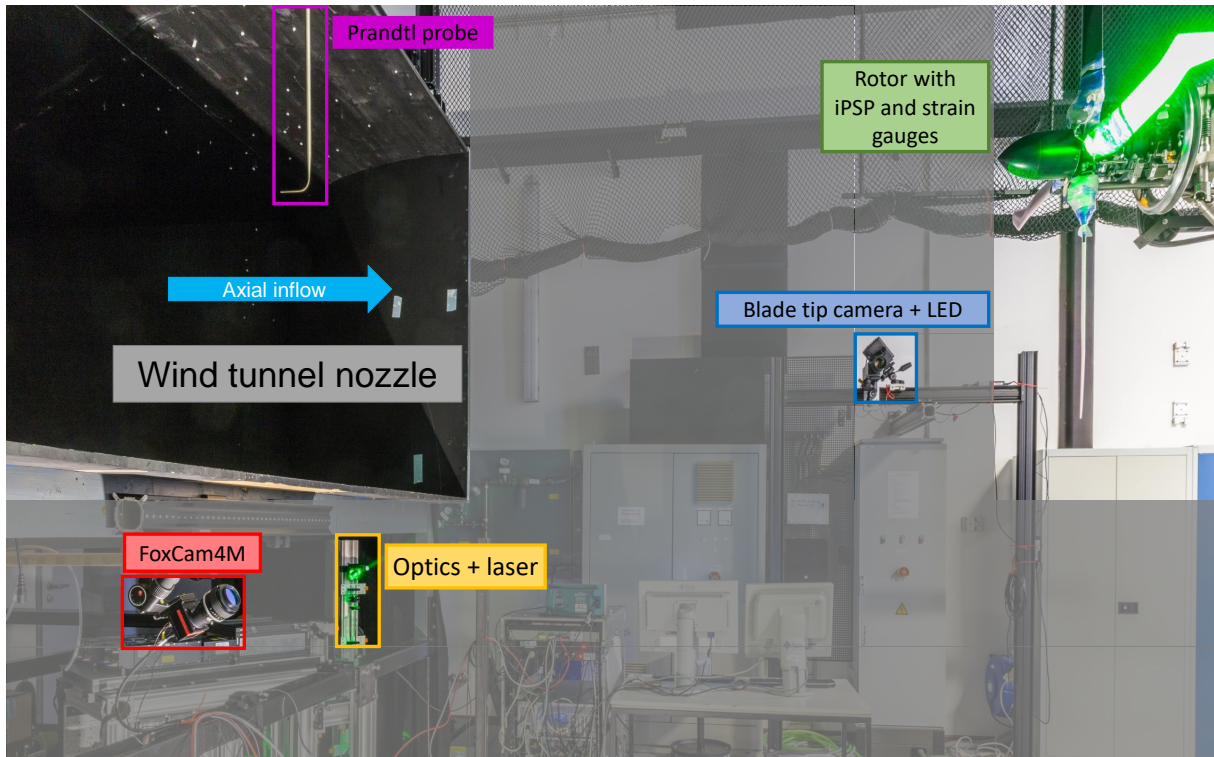


Figure 1. Image of experimental setup at the RTG in Göttingen

m × 3.4 m (height × width). The entire measurement was carried out at an axial inflow velocity of $v_\infty = 2$ m/s. The axial inflow is intended to prevent blade vortex interaction and the recirculation of blade tip vortices. In the RTG, a generic test case comparable to climb is represented. Additionally, dynamic stall can be investigated in isolation from all other main rotor effects, like lateral flow, compression shocks and blade vortex interaction (BVI). The double-swept rotor blades were developed and designed at DLR-AE by Müller (Ref. 25) and inspired by the ERATO-blade (Refs. 29, 30). The aerodynamic airfoil of the rotor blades are in a range from $0.25 \leq r/R \leq 1$. The two parallel outer surfaces of the rotor blade clamping are referred to as the blade root, see Fig. 3. The rotor has a radius of $R = 0.652$ m and the chord length tapers over the radius from $c_{\text{root}} = 0.072$ m at the root to $c_{\text{tip}} = 0.020$ m at the blade tip. This consequently leads to a blade tip that is much softer in bending and torsion. The radial torsion runs from -1.2° at the root to -10.5° at the blade tip. For more information about radial sweep and twist distribution as well as aerodynamic and structure design, see Ref. 25.

In this experimental setup, the laser and the corresponding optics for the exposure of the iPSP-coated rotor blade were placed right below the wind tunnel nozzle (Fig. 1). The camera required for the iPSP (FoxCam4M) was placed below the wind tunnel nozzle, approximately aligned with the blade in measurement position and orthogonally facing the blade suction side at approximately the median angle of incidence. For more information about the iPSP setup, see Ref. 27. The axial

inflow was measured using a Prandtl-probe in the nozzle. The blade tip camera as well as the flash LED were placed with a horizontal view on the blade tip as seen in Fig. 1. The RTG has a swashplate which allows both collective and cyclic pitch settings. Additionally, the RTG has a mechanism to rotate the usually stationary part of the swashplate 360° during operation. This allows to scan an entire pitch cycle at a fixed azimuthal position. For more information about the swashplate mechanism, see Ref. 20, 23. The pitch angle of the blade root can be described by

$$\Theta_{\text{root}} = \bar{\Theta}_{\text{root}} - \hat{\Theta} \cdot \cos(2\pi t f_{\text{rotor}}), \quad (1)$$

where $\bar{\Theta}_{\text{root}}$ is the collective-pitch angle of all rotor blades and $\hat{\Theta}$ is the cyclic-pitch amplitude. The blade root pitch angle is measured via Hall sensors in the blade mounts. The investigated cyclic pitch cases are listed in Tab. 1. All test cases were measured under the following conditions: $f_{\text{rotor}} = 23.6$ Hz, $v_\infty = 2.0$ m/s, $M_{\text{tip}} = 0.282 - 0.285$ and $Re_{\text{tip}} = 5.84 - 5.95 \times 10^5$.

Table 1. Cyclic test cases

Test Case	$\bar{\Theta}_{\text{root}}, ^\circ$	$\hat{\Theta}, ^\circ$
C1	17	8
C2	27	6
C3	30	6

In Fig. 2 it can be seen that each blade is equipped with a dif-

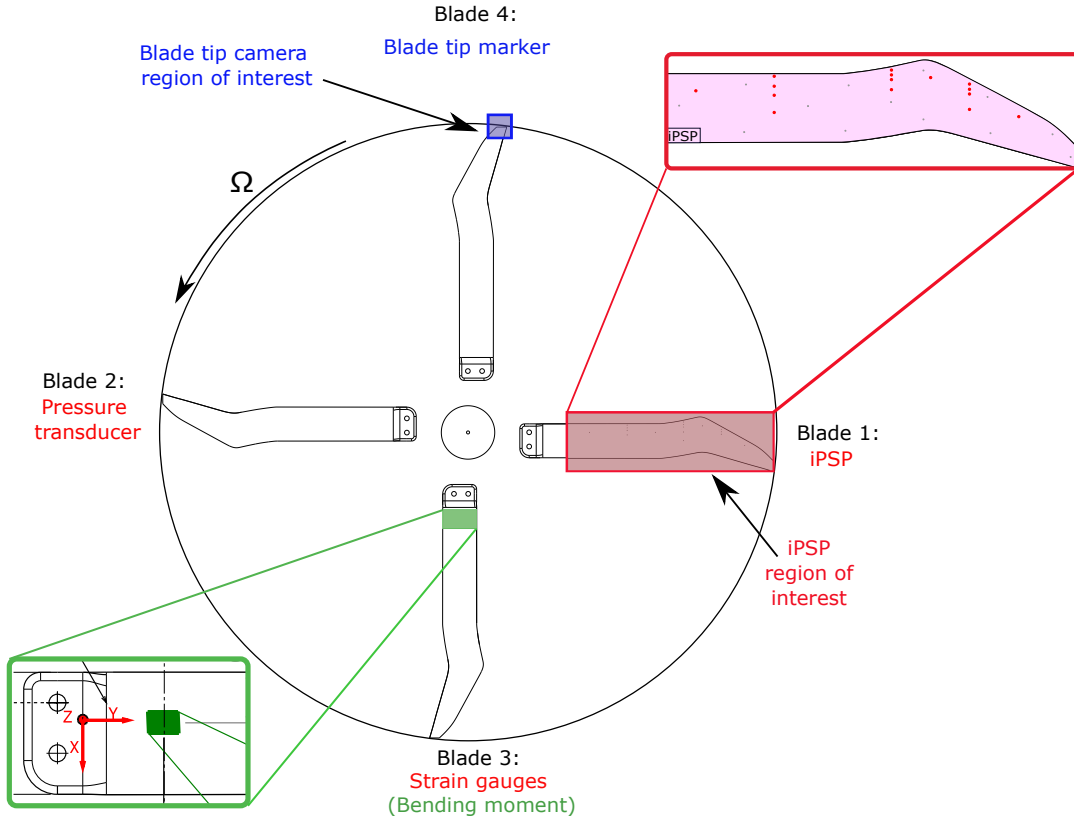


Figure 2. Overview of the applied measurement techniques on the rotor blades

ferent measurement technique. For the comparison of the different techniques (e.g. blade tip camera, iPSP, strain gauges and pressure sensors) with each other, it is assumed that the aerodynamic behavior as well as the flap displacement are the same for the corresponding blades. In order to compare the results from the different measurement techniques, all data were recorded simultaneously and synchronized using the pitch setting recordings of the respective blades.

Strain gauges

Strain gauges were used to measure the integral blade bending moment as well as the flap displacement. For the measurement of the integral blade bending moment at the root, strain gauges were glued at $0.3R$ and $0.35c$ (related to the center of the strain gauges) on the surface of the rotor blade, see Fig.3. The two strain gauges were positioned on the upper and lower side at the same radial and chordwise location, see Fig.3. The measuring grids were parallel to the leading edge at the blade root. The coordinate system shown in Fig.3 defines the exact reference point at the blade root in radial and chord direction with respect to the bending moment. In relation to the rotor blade cross-section, the bending moment acts lateral to the chord in z -direction, see Fig.5. As measurement type a half bridge with added equivalent resistors at one of the blades was used. Sensors of type 1 – LY11 – 6/350 from HBM were used as strain gauges, with a nominal resistance of 350Ω . For the equivalent resistors a SMD precision resistor with a deviation tolerance of 0.01% was used. The adhesive was the X60 from HBM due to its low thermal conductivity, in order to keep the temperature influence on the measuring bridge low, since a half bridge is not temperature compensating. However, due to the bridge circuit principle, a half bridge is the best opportunity to measure the blade bending moment, since this is dependent on the absolute strain. For the positioning of the strain gauges, finite element (FE) calculations were performed in advance to determine the strain flow close to the blade root. The optimum position for the measuring bridge was then derived from these calculations.

For the calibration procedure according to Ref.28, defined loads were applied at defined radial positions. The integral blade bending moment was calibrated from 58 Nm to -58 Nm . For this purpose, three calibration brackets were mounted to the rotor blade at different radial positions in order to apply

a line load, see Fig.6. The calibration of the strain gauges was carried out with mounted blades at the rotor. Since the rotor plane is aligned vertically, the calibration weights were applied to the calibration brackets with ropes and guided over aligned pulleys. The point of force application can be adjusted in chord direction on the calibration brackets for each radial position. In order to be able to apply a bending moment without any blade torsion at each combination of radial line loads, it is necessary to place the force application point in the shear centers at the three radial positions of the airfoil profile molds, see Fig.6. To achieve this, the force application point in the chord direction for the bending moment was set for each radial section in such a way that there was no blade tip torsion.

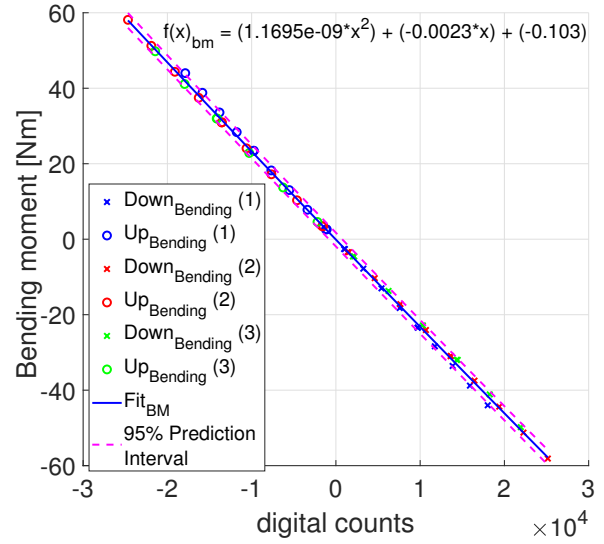


Figure 4. Bending moment over digital telemetry counts

This made it possible to apply decoupled line loads for the bending moment on the elastic axis. For coupled line loads, the force application point was shifted out of the elastic axis for each radial section. This procedure provides the calibration function of the strain gauge measuring bridge. In Fig.4, the bending moment is plotted as a function over the digital telemetry counts. The designation $Up_{Bending}$ in the plotted legend defines

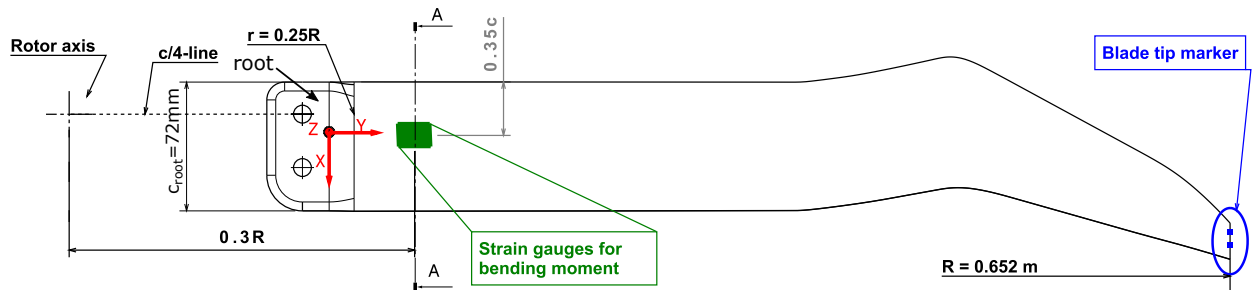


Figure 3. Rotor blade planform and position of strain gauges and blade tip marker

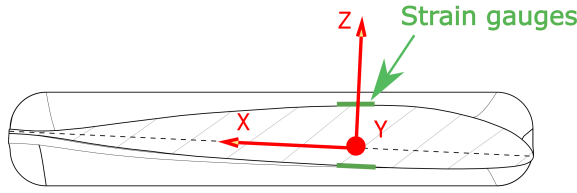


Figure 5. Crosssection A-A of Fig. 4

a bending up of the rotor blade in z-direction (Fig. 5) at positive bending moment and negative digital counts. Conversely, $Down_{Bending}$ defines a downward bending of the rotor blade (negative z-direction) at negative bending moment and positive digital counts. The different colors define several calibration series with the same load combination to ensure reproducibility. A linear strain behavior over the measuring range must be ensured for the strain gauges. The calibration curve was approximated using the denoted second order polynomial in Fig. 4. The narrow bandwidth (± 2 Nm) of the 95 % confidence interval of the quadratic fit shows a good repeatability of the calibration. In addition to calibrating the bending moment, the displacement of the blade tip was measured for all applied load combinations, coupled and uncoupled. In this way, the blade root strain gauges were additionally calibrated for displacement. The calibration curve for the flap displacement via the strain gauges have a similarly good accuracy of the approximation polynomial as the integral bending moment. The telemetry used to sample the strain gauges has a signal bandwidth of 19 kHz. For the evaluation of the cyclic pitch cases, phase averaged values over approx. 3600 periods are used.

Blade tip marker

The blade tip markers are used for measuring flap displacement. For this purpose, two retroreflective markers are glued to the face of the blade tip (see Fig. 3) and images are recorded using a PCO Sensicam camera and a flash LED. All blade tip marker images are taken at a fixed azimuthal position of the

rotor blade. To achieve sufficient image sharpness of the rotating blade tip, the image is illuminated by a LED flash for $\tau_{bt} = 7\mu s$. The two markers have a distance of $d = 7.6$ mm from each other. For the calibration of the blade tip images, a calibration target with defined geometry was held into the image to determine the magnification factor. The displacement of the marker images under loads is evaluated with respect to a reference image to derive the flap displacement. For this purpose, the centroid of the markers is determined with a algorithm. In order to shift the entire period of a pitch oscillation through the fixed azimuthal measurement window, the stationary part of the swash plate is rotated by 360° and thus one oscillation period is shifted through the fixed measurement window, see Ref. 23 for more details. One image is recorded every second revolution. In total, an entire cyclic-pitch period is resolved with 1300 blade tip images. Thus, the period of a pitch cycle can be resolved with 0.28° azimuth.

Pressure-transducer and pressure-sensitive paint

The surface pressure distribution was measured by two different techniques. The surface pressure distribution is measured at discrete positions on the suction side of the airfoil using pressure-transducers. On the other hand, unsteady pressure-sensitive paint is used for the measurement of the spatially resolved pressure distribution. For the surface pressure measurement by means of pressure-transducers, one rotor blade is equipped with 15 sealed gauge unsteady pressure transducers of the type *Kulite LQ-062*. The pressure transducers are radially divided into six different sections. The exact position can be found in Tab. 2. r/R indicates the radial position and x/c the chord-wise position from the leading-edge. The pressure transducers are relatively encapsulated at 76.5 kPa and have a pressure range of ± 70 kPa. The maximum static acceleration that can be sustained is 1000 g. For calibration, the rotor blade was enclosed pressure-tight from the blade tip to the root by two planform-milled half-shells made of acrylic glass. The half-shells were pressed together by several screw connections. The root area was sealed using plasticine and an

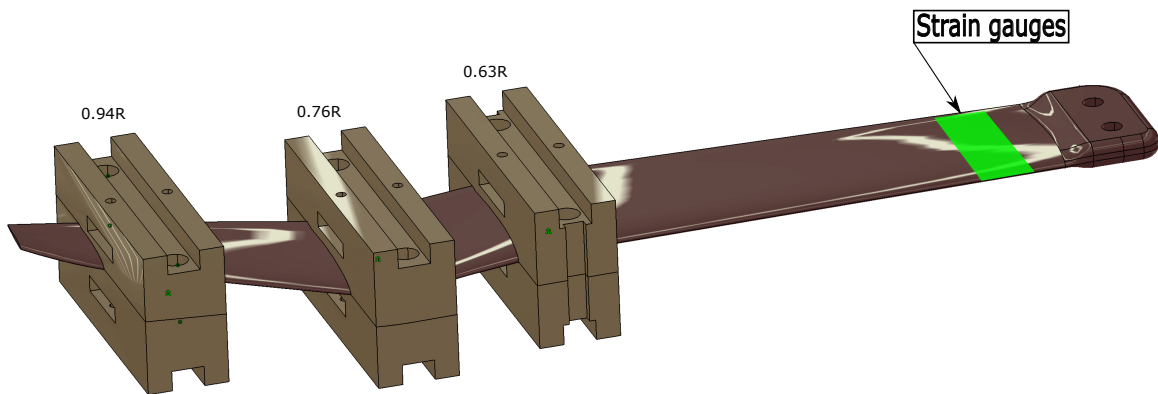


Figure 6. Rotor blade with radial mounted calibration brackets

elastomer (see Fig.7). The pressure sensors were calibrated from 140 kPa to 6.5 kPa in 5 kPa increments.

Table 2. Positioning of the pressure-transducers

r/R	0.40	0.52	0.71	0.77	0.83	0.90
x/c	0.251	0.042	0.049	0.0251	0.094	0.251
		0.192	0.124		0.178	
		0.321	0.195		0.261	
		0.545	0.337		0.571	

All pressure sensors were measured using a telemetry system, which has a signal bandwidth of 19 kHz. For the evaluation of the cyclic pitch cases, phase averaged values over approx. 3600 periods are used.

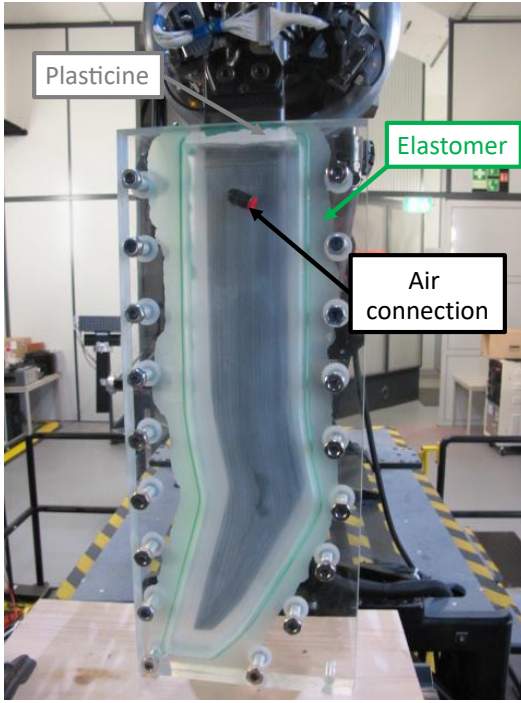


Figure 7. Calibration mold for pressure transducers

A different blade, not instrumented with Kulites, was equipped with unsteady pressure sensitive paint in the range between $0.35 \leq r/R \leq 1$, see Fig.2. A detailed explanation of the measurement technique, the applied iPSP sensor, the experimental setup and the data reduction is presented in Ref.27. Therefore, only a brief summary is given here. The employed iPSP sensor provides unsteady surface pressures with a -3dB cutoff frequency of 6kHz (Refs. 31, 32). At the tested rotating frequency of 23.6 Hz, the time response corresponds to an averaging across an equivalent azimuthal angle of 1.4° . The iPSP was excited at 532 nm by a laser system (Quantel Evergreen 200) providing 400 mJ/pulse. Pressures were obtained using the so-called “single-shot lifetime” method, see (Refs. 33, 34), where the unsteady surface pressure, i.e. the luminescent decay of the iPSP sensor, is captured by two successively acquired images after excitation using a single-shot of laser light. For image acquisition, an inhouse devel-

oped camera (FoxCam4M) was used (Refs. 35, 36) which allows the acquisition of two images in direct succession with both exposures limited to several microseconds only. That way, rotational image blur was reduced to less than 2 % of the root chord at a blade tip speed of 96.7 m/s. Due to the limited repetition rate for laser (15 Hz) and camera (20 Hz for double frame acquisition), the rotation speed of the swash plate was adopted that a total of 1600 double frames were recorded every second blade revolution during the entire pitch cycle. The resulting phase resolution of iPSP data was $1/1600$, i.e. 0.225° azimuth. The iPSP results presented in this paper display phase-consecutive averages of 50 single-shot results, which corresponds to an average across 11.25° azimuth.

RESULTS

In the following, aeroelastic and aerodynamic results are presented for the three test cases representing attached flow, light and deep dynamic stall, respectively. The surface pressures are expressed as $C_p M^2$ according to

$$C_p M^2 = \frac{p - p_\infty}{\rho_\infty / 2 \cdot a_\infty^2}, \quad (2)$$

where ρ_∞ is defined as air density of the axial inflow. a_∞ is the speed of sound of the axial inflow, p_∞ is the pressure of the axial inflow and p is the local measured pressure on the surface. The pressure coefficient C_p and Mach number M are defined as

$$C_p = \frac{p - p_\infty}{\frac{\rho_\infty}{2} u^2} \quad \text{and} \quad M = \frac{u}{a_\infty}, \quad (3)$$

here u is the rotation speed at the respective radial position. The aeroelastic results are presented as flap displacement, blade pitch angle Θ_{root} and integral blade bending moment against the pitch phase and flap displacement against blade pitch angle (e.g. Fig.9 a and b). For the cyclic cases $\Theta_{root} = 27^\circ \pm 6^\circ$ (Fig.11) and $\Theta_{root} = 32^\circ \pm 6^\circ$ (Fig.13), the representations of flap displacement, blade pitch angle (Θ_{root}) and bending moment is analogous to Fig.9. The blade pitch angle Θ_{root} represents the blade pitch oscillation, the integral blade bending moment represents the excitation moment, and the flap deformation represents the blade response. The phase positions of the depicted surface pressure (Fig.10, 12, 14) selected on the basis of significant points in the evolution of the tip displacement and integral bending moment (e.g. maximum flap displacement).

Flap displacement

In Fig.8 the flap displacement calculated from the strain gauges is compared to the result of the flap displacement from the blade tip camera against the pitch phase for C1, C2, and C3. For all test cases, both measurement techniques yield similar results with only minor differences. These are mainly seen during downstroke of the test cases C2 and C3 when the flap displacement increases again, see Fig.8 ($0.6 \leq t_{rotor} \leq 0.75$).

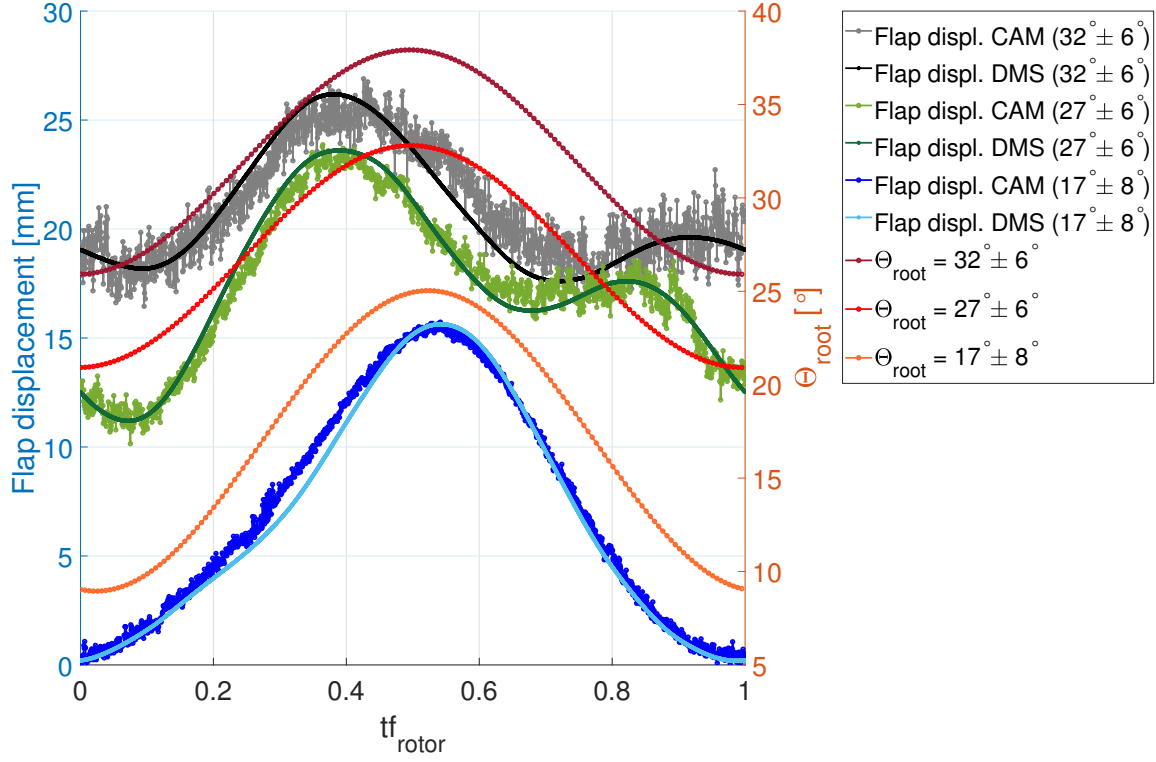


Figure 8. Flap displacement (strain gauges and blade tip camera) and pitch angles against the pitch phase for all cyclic test cases

The maximum deviation for C3 is 0.8 mm between both measurement techniques at $tf_{rotor} = 0.62$ during downstroke. For C2 the maximum deviation is 0.5 mm also during downstroke at $tf_{rotor} = 0.72$. C1 has a maximum deviation of 0.3 mm during upstroke at $tf_{rotor} = 0.36$. Thus, the deviation between both measurement techniques increases only slightly with increasing strength of the dynamic stall. A clear deviation in the flap displacement between C1 and C2, C3 can be seen. With increasing collective-pitch the development of a non-linear behavior in the flap displacement with respect to the pitch oscillation over phase can be recognized. This behavior increases with increasing strength of the dynamic stall. The causes of this flap displacement behavior in terms of global surface pressures and integral blade bending moments are discussed below.

Test case C1

In Fig. 9 a, the flap displacement, blade pitch angle Θ_{root} (red) and integral bending moment (green) are plotted against the pitch phase. For the flap displacement the raw data (dotted blue) as well as smoothed curves using a Savitzky-Golay filter (cyan) are depicted. Fig. 9 b shows the flap displacement (blue) against the blade pitch angle. For the cyclic-pitch case C1, the flap displacement qualitatively follows the pitch oscillation. The maximum flap displacement of 15 mm is reached at the maximum root pitch angle of $\Theta_{root} = 24.8^\circ$. Only a slight hysteresis effect of the flap displacement against the blade pitch angle between upstroke and downstroke can be

recognized (Fig. 9 b). An almost identical behavior can be seen in the evolution of the integral bending moment at the blade root, see Fig. 9 a. The bending moment corresponds well with the flap displacement over the phase. Both, excitation moment (i.e. the integral bending moment) and the blade response (flap displacement), reach their maximum at approximately the phase corresponding to the maximum pitch angle ($\Theta_{root} = 25^\circ$). This indicates a linear behavior between the excitation moment and the blade response for C1. Thus, blade pitch oscillation (Θ_{root}), excitation moment (integral bending moment) and blade response (flap displacement) corresponds with each other. The flap displacement follows the blade pitch oscillation without delay and deviation in evolution. Furthermore, no significant phase shift between the excitation moment (bending moment) to blade response (flap displacement) over phase indicates an ideally stiff rotor blade (Refs. 37, 38). In Fig. 10 (left), the surface pressures measured with iPSP are shown for five different pitch angles during the pitch cycle C1 with $\Theta_{root} = 17^\circ \pm 8^\circ$. Corresponding chord-wise cuts at four radial positions are plotted on the right hand side of Fig. 10, where the pressure transducer data are compared against the iPSP results. For C1, at $\Theta_{root} = 13^\circ$ (Fig. 10 a) in the upstroke, a slight suction peak close to the blade tip at the leading edge can be seen in iPSP (left) and pressure sensor data (right). With increasing pitch angle an decrease of the pressure coefficients (iPSP and pressure sensors), on the backward swept part of the rotor blade at $r/R = 0.83$ and $r/R = 0.90$ can be seen (Fig. 10 b and c).

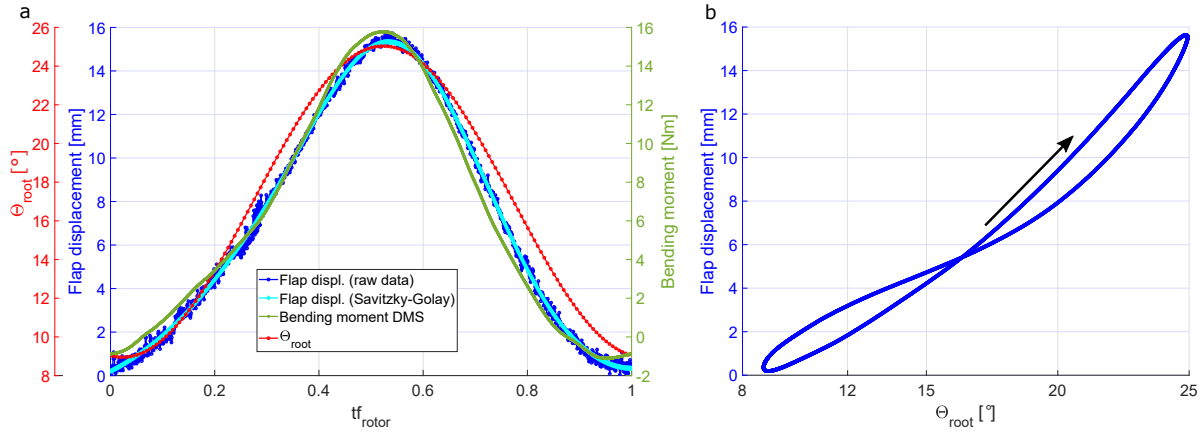


Figure 9. Flap displacement, blade pitch angle and integral blade bending moment against the pitch phase (a) and flap displacement against blade pitch angle (b) for $\Theta_{root} = 17^\circ \pm 8^\circ$

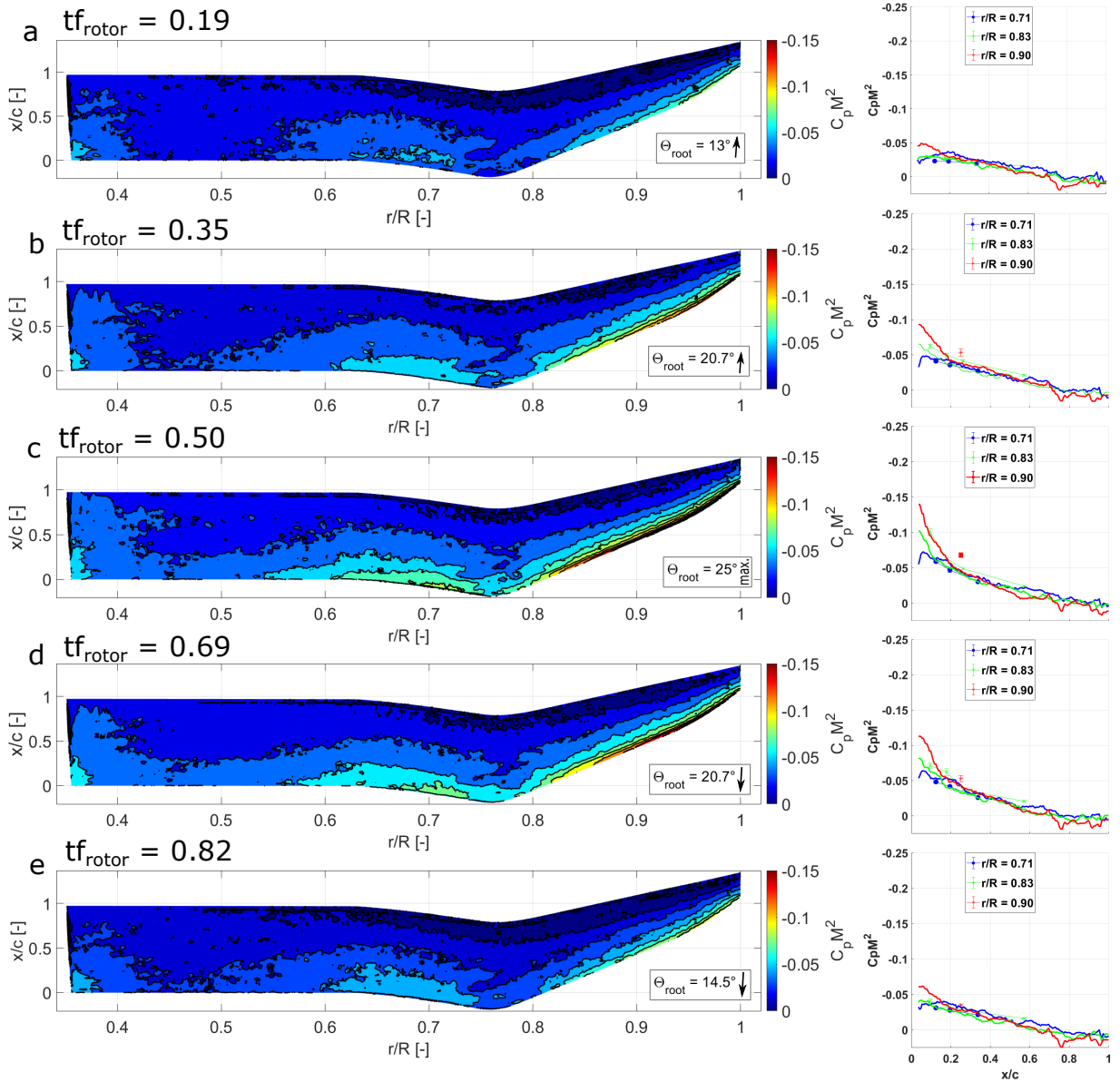


Figure 10. Ensemble averaged surface pressure maps as $C_p M^2$ at indicated cyclic-pitch positions and corresponding pressure coefficients against streamwise coordinate x/c from iSP and pressure transducers for $\Theta_{root} = 17^\circ \pm 8^\circ$

Along the leading edge of the backward swept part of the rotor blade the growth of a suction peak can be observed. This suction peak between blade tip and apex grows with increasing pitch angle (Fig. 10 a - c). For the displayed pitch angles, the pressure coefficients reach their minimum at $\Theta_{root} = 25^\circ$. As expected, the phase corresponding to maximum lift roughly coincides with the phases of maximum integral bending moment and flap displacement (see Fig. 9 a). This is also evident in the case of integral bending moment and flap displacement, see Fig. 9 (right). Thus, all measured data (integral bending moment, flap displacement and pressure data) show a good qualitative evolution over phase at the point of maximum lift force. When reaching $\Theta_{root} = 25^\circ$, there are no regions showing stall characteristics, neither on the forward nor on the backward swept part of the rotor blade. During downstroke, there are only slight deviations from the upstroke in the pressure data (Fig. 9 b). At $\Theta_{root} = 20.7$, slightly higher pressure coefficients (Fig. 10 d right) can be seen at the forward and backward swept part of the rotor blade than at $\Theta_{root} = 20.7^\circ$ during the upstroke (Fig. 10 b right). At $\Theta_{root} = 14.5^\circ$ during downstroke (Fig. 10 e), the pressure distribution shows a very similar distribution to $\Theta_{root} = 13^\circ$ (Fig. 10 a) during upstroke.

Test case C2

For test case C2, a significant deviation between the blade pitch oscillation (Θ_{root}) and flap displacement can be seen (Fig. 11 a). The flap displacement and integral bending moment reveal a strongly non-linear behavior compared to the blade pitch oscillation (Θ_{root}). This is represented by the formation of a saddle point during downstroke in the flap displacement and integral bending moment (Fig. 11 a). The curves of flap displacement and integral bending moment are again in phase (Fig. 11 a). Thus, there is no phase shift between the excitation moment (integral bending moment) and the blade response (flap displacement), which supports the assumption of an ideally stiff rotor blade. In addition, it can be seen that, unlike in test case C1, the maximum flap displacement (23.6 mm) and the maximum integral bending moment (21.7 Nm) are already reached before the maximum pitch angle. When the maximum pitch angle ($\Theta_{root} = 33^\circ$) is reached, the flap displacement and the integral bending moment already sharply drop (Fig. 11 a). From $tf_{rotor} = 0.74$, however, there is a turning point in the drop of flap displacement and integral bending moment. Here, a renewed increase of both quantities can be seen, which reaches its maximum at $tf_{rotor} = 0.74$ (Fig. 11 b). In the range of $\Theta_{root} = 23.2^\circ$, a slightly increased fluctuation in the raw data of the blade tip camera is observed, which may indicate a detachment or reattachment process. After $\Theta_{root} = 23.2^\circ$ ($0.9 \leq tf_{rotor} \leq 1.0$), the flap displacement and the integral bending moment decrease again. The saddle point in the flap displacement is also apparent in Fig. 11 b as a stronger expression of the hysteresis against the blade pitch angle. In addition, Fig. 11 b shows a light stall behavior in the flap displacement.

Analogous to Fig. 10, the surface pressure data are shown in

Fig. 12. On closer inspection, these data provide an explanation for the non-linear behavior of the flapping motion. For $\Theta_{root} = 24.1^\circ$, a pronounced suction peak can be seen at the backward swept part of the rotor blade, from the blade tip to the apex. In addition, a suction peak in the area of the forward swept part can be seen in Fig. 12 a. When the maximum flap displacement and integral bending moment at $\Theta_{root} = 29.8^\circ$ are reached, the first stall phenomena appear in the $C_p M^2$ distribution in the area of the blade tip (Fig. 12 b). This incipient stall is initiated by the inward migration of detaching the blade tip vortex, see (Ref. 27). However, when looking at the pressure coefficients in chord direction, strong suction peaks at $r/R = 0.71$, $r/R = 0.83$ and $r/R = 0.90$ can be seen (Fig. 12 b right). When the maximum pitch angle is reached, it can be seen that a large part ($0.9 \leq r/R \leq 1$) of the backward swept area of the rotor blade already shows flow separation (Fig. 12 c left). This can also be seen in the drop of the flap displacement and integral bending moment (Fig. 11 a) as well as in the breakdown of the suction peak at $r/R = 0.90$ in Fig. 12 c. At $\Theta_{root} = 24.6^\circ$ during downstroke, the flap displacement and the integral bending moment start to increase again. At this blade pitch angle, both the global $C_p M^2$ distribution and the $C_p M^2$ distribution in chord direction reveal a reattachment of the flow up to the blade tip (Fig. 12 d and e). This again results in strong suction peaks, especially on the backward swept part of the rotor blade, which leads to an increase in lift and thus to a renewed increase in the flap displacement. A comparison of the $C_p M^2$ distribution during upstroke (Fig. 12 a and b) and downstroke (Fig. 12 d and e) indicates that the detachment and reattachment processes take place at different pitch angles and thus with a time lag. At $\Theta_{root} = 23.2^\circ$ (downstroke), the forward and backward swept parts of the rotor blade again reveal a fully attached flow, with similarly strong suction peaks as at $\Theta_{root} = 26.4^\circ$ (downstroke). For this cyclic-pitch case C2 it can be seen that during the whole pitching oscillation no stall characteristics appear on the forward swept part of the rotor blade. The detachment and reattachment processes affect the backward swept part of the rotor blade only.

Test case C3

The cyclic-pitch case C3 reveals a very similar behavior to C2 with respect to the flap displacement and the integral bending moment, see Fig. 13 a. As with C2, a renewed increase in flap displacement and integral bending moment can be seen, see Fig. 13 at ($0.78 \leq tf_{rotor} \leq 1.0$). In this case, however, the renewed increase of the flap displacement during downstroke is much more pronounced than for C2 (Fig. 11 a). The evolution of the flap displacement rather approaches a 2/rev oscillation with a significantly lower second increase of the flap displacement for C3. The deviation from blade pitch oscillation (Θ_{root}) to flap displacement already described for C2 also becomes clear (Fig. 13 a). The 2/rev oscillation with a significantly lower second increase of the flap displacement is also depicted in Fig. 13 b by a much stronger expression of the hysteresis against the blade pitch angle than for C2.

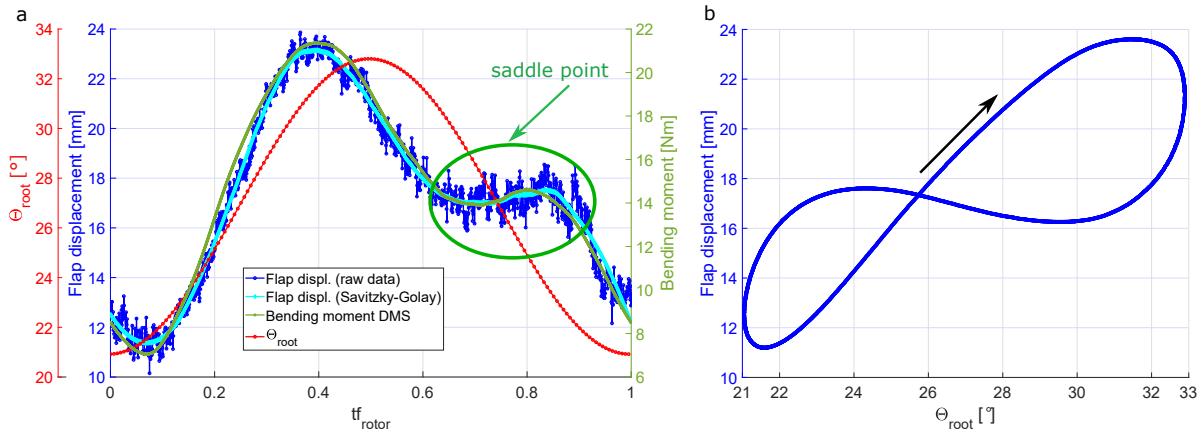


Figure 11. Flap displacement, blade pitch angle and integral blade bending moment against the pitch phase (a) and flap displacement against blade pitch angle (b) for $\Theta_{root} = 27^\circ \pm 6^\circ$

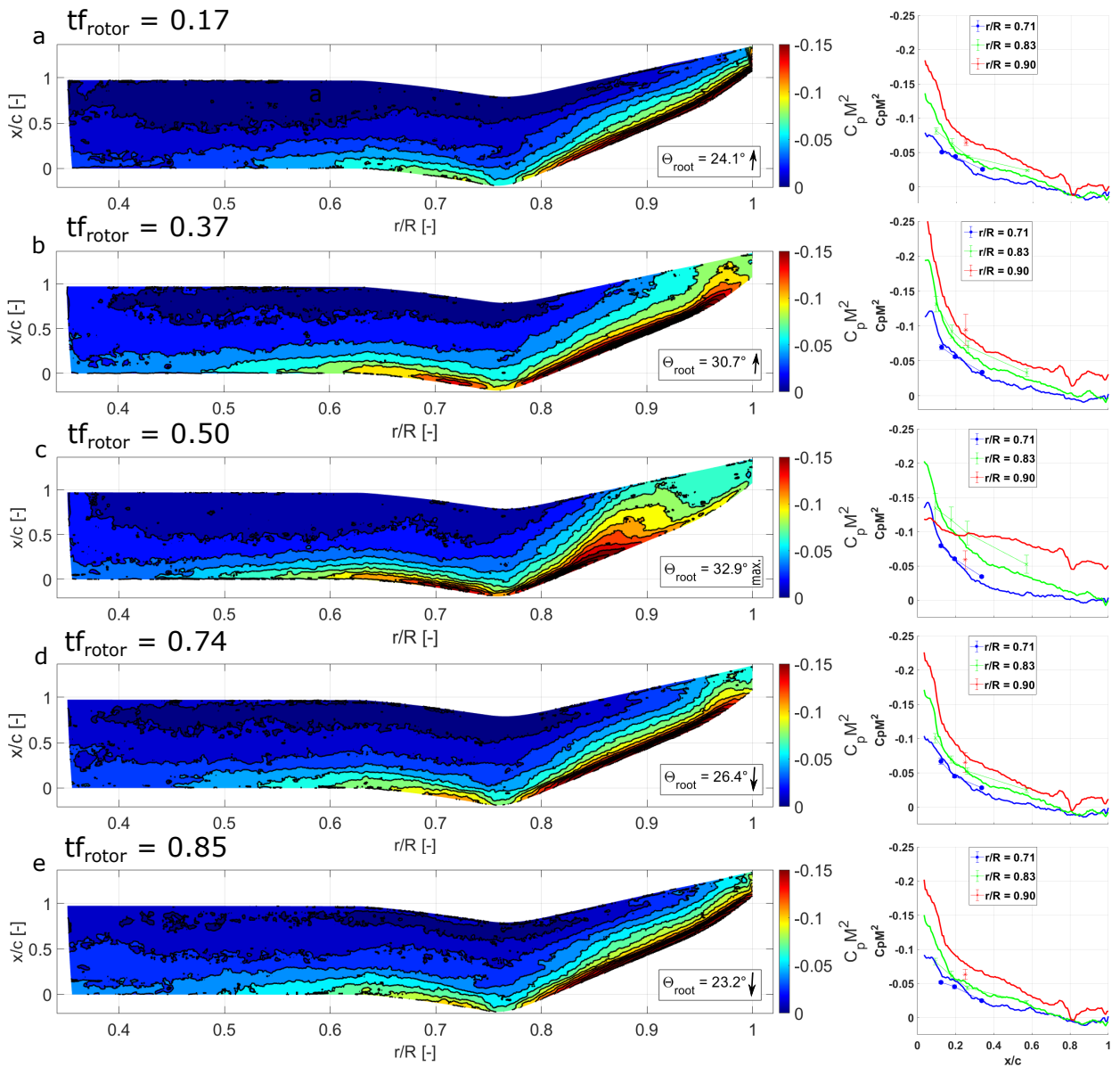


Figure 12. Ensemble averaged surface pressure maps as $C_p M^2$ at indicated cyclic-pitch positions and corresponding pressure coefficients against streamwise coordinate x/c from iSP and pressure transducers for $\Theta_{root} = 27^\circ \pm 6^\circ$

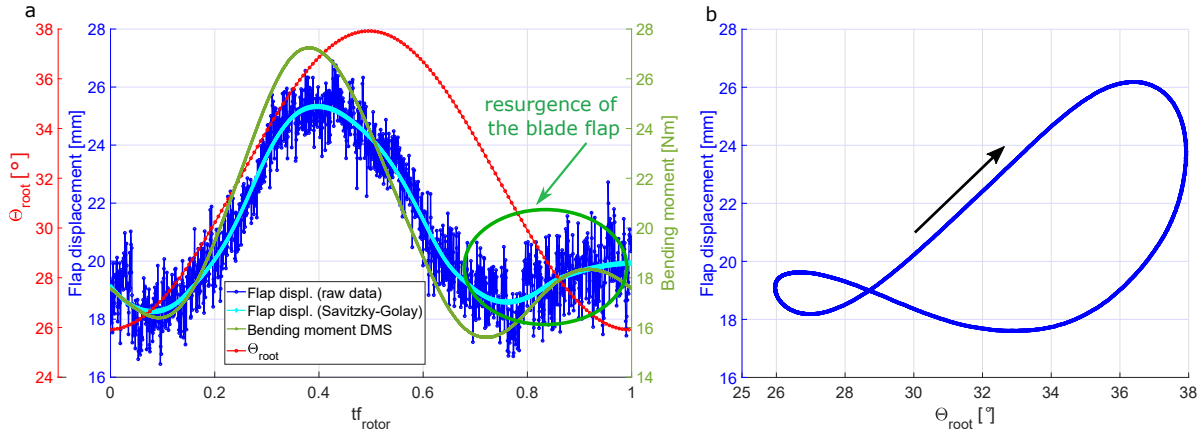


Figure 13. Flap displacement, blade pitch angle and integral blade bending moment against the pitch phase (a) and flap displacement against blade pitch angle (b) for $\Theta_{root} = 32^\circ \pm 6^\circ$

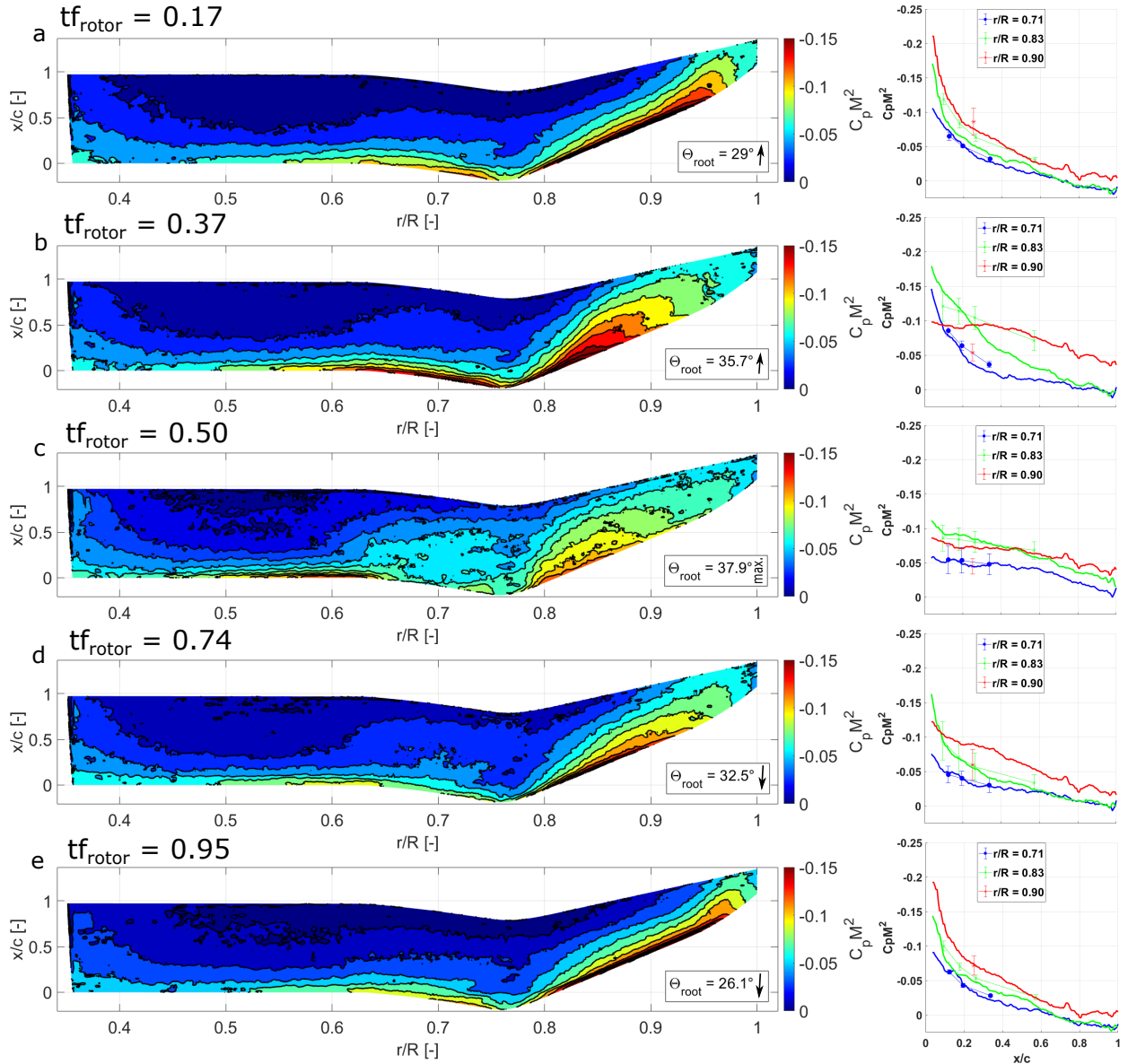


Figure 14. Ensemble averaged surface pressure maps as $C_p M^2$ at indicated cyclic-pitch positions and corresponding pressure coefficients against streamwise coordinate x/c from iSP and pressure transducers for $\Theta_{root} = 32^\circ \pm 6^\circ$

In addition, Fig. 13 b shows a typical deep stall behavior in the flap displacement. The $C_p M^2$ results, both the global distribution and the chord-wise cuts, reveal significant differences between the test cases C2 and C3 (Fig. 12 and Fig. 14). For C3, already at the beginning of the upstroke at $\Theta_{root} = 29^\circ$, first stall phenomena appear in the area of the blade tip, but there are still strong suction peaks both inboard and outboard of the apex, see Fig. 14 a. When reaching the maximum flap displacement (25.5 mm) and the maximum integral bending moment (27.2 Nm) at $tf_{rotor} = 0.37$, a region of detached flow can be recognized between $0.88 \leq r/R \leq 1.0$ (Fig. 14 b). At this pitch angle phase, flow detachment is also indicated by the collapsing suction peak of $C_p M^2$ at $r/R = 0.9$ in Fig. 14 b. The surface pressure results at the maximum pitch angle ($\Theta_{root} = 37.8^\circ$) indicate a broad flow separation, both inboard and outboard of the apex. The resulting decrease in lift is also represented by the decreasing flap displacement and integral bending moment in Fig. 13 a. At $tf_{rotor} = 0.74$, the flap displacement and the integral bending moment increase again (Fig. 13 a). This is also reflected in the $C_p M^2$ distribution at $\Theta_{root} = 32.5^\circ$, which indicates reattached flow at the forward swept area and partial reattachment in the backward swept part of the blade, see Fig. 14 d. At $\Theta_{root} = 26.1^\circ$, the flow is completely reattached in the backward swept part (Fig. 14 e). As opposed to the case C2, flow separation can also be detected inboard of the apex in the forward swept part of the blade for case C3. This eventually leads to a "deep dynamic stall" behavior, which is characterized by a stronger increase of the renewed rise of the flap displacement during downstroke.

CONCLUSIONS

The study presents the first investigation of dynamic stall on a four-bladed rotor with an innovative double-swept blade tip with a focus on both the aeroelastic behavior and the underlying aerodynamics. Integral blade bending moment and blade flapping were measured using strain gauges. The flap displacement was also measured optically by tracking blade tip markers. Unsteady surface pressures were recorded using unsteady PSP across the outer 65% of the blade span and fast response pressure transducers. The major outcomes of the study can be summarized as follows:

1. The blade bending moment shows a good qualitative agreement over phase with the flap displacement. The blades can be assumed to be ideally stiff since no relevant phase shift between maximum flap displacement and maximum bending moment could be detected.
2. For two of the examined test cases (C2 and C3), the flap displacement and blade bending moment experience strong non-linearity with respect to the pitch angle oscillation. During downstroke, a saddle point (C2) or a 2/rev oscillation with a significantly lower second increase of the flap displacement (C3) is seen.
3. The non-linearity in the flap displacement and bending moment during downstroke increases with increasing strength of the dynamic stall.

4. The surface pressure results indicate a phase-shifted separation and reattachment of the flow between the forward and backward swept part of the rotor blade. The flow separation starts first at the blade tip on the backward swept part of the rotor blade.
5. The iPSP results for case C3 indicate a larger stalled flow area on the rotor blade as opposed to C2 with flow separation not only outboard, but also inboard of the apex. A direct link could be established between the increased extent of flow separation and the resulting amplification of the non-linear behavior between integral blade bending moment and flap displacement with respect to the pitch oscillation.

ACKNOWLEDGMENTS

Funding of the DLR project URBAN Rescue is gratefully acknowledged. The authors would like to thank T. Büte and M. Krebs (DLR Göttingen) for all support in the measurement campaign and C. Stieg (DLR Göttingen) for his support in model preparation.

REFERENCES

1. McCroskey, W. J., "The phenomenon of dynamic stall.," *Technical memorandum 81264, NASA Ames Research Center, Moffett Field, CA*, 2016, 1981.
2. Leishman, J. G., "Principles of Helicopter Aerodynamics,," *Cambridge University Press, second edition*, 2006.
3. Lütke, B., Nuhn, J., Govers, Y., and Schmidt, M., "Design of a rotor blade tip for the investigation of dynamic stall in the transonic wind-tunnel Göttingen,," *The Aeronautical Journal*, Vol. 74:(1232), 2016.
4. Lütke, B., "Dynamic Stall on a Pitching Double-Swept Rotor Blade Tip,," *Diss., Technische Universität München*, 2017.
5. Hebler, A., Schojda, L., and Mai, H., "Experimental investigation of the aeroelastic behaviour of a laminar airfoil,," *International Forum on Aeroelasticity and Structural Dynamics (IFASD)*, 24-26 June, Bristol, 2013.
6. Braune, M. and Hebler, A., "Mechanisms of Transonic Single Degree of Freedom Flutter of a Laminar Airfoil,," *International Forum on Aeroelasticity and Structural Dynamics (IFASD)*, 9-13 June, Savannah, Georgia, 2019.
7. Wiggen, S., "Bewegungsinduzierte instationäre Luftkräfte bei wirbeldominierter Strömung,," *Diss., Technische Universität Carolo-Wilhelmina zu Braunschweig*, 2016.
8. Braune, M. and Koch, S., "Application of hot-film anemometry to resolve the unsteady boundary layer transition of a laminar airfoil experiencing limit cycle oscillations,," *Experiments in Fluids*, Vol. 61(68), 2020, <https://doi.org/10.1007/s00348-020-2907-y>.

9. Visbal, M.R. and Garmann, D.J. , “Numerical Investigation of Spanwise End Effects on Dynamic Stall of a Pitching NACA 0012 Wing,” *AIAA SciTech Forum*, 9-13 January, Grapevine, Texas, 2017.
10. Benton, S.I. and Visbal, M.R., “The onset of dynamic stall at a high, transitional Reynolds number,” *Journal of Fluid Mechanics*, Vol. 861, 2018, pp. 860–885, doi:10.1017/jfm.2018.939.
11. Carr, L.W, “Progress in Analysis and Prediction of Dynamic Stall,” *Journal of Aircraft*, Vol. 25(1), 1988, pp. 06–17, doi:10.2514/3.45534.
12. Leishman, J.G., “Dynamic stall experiments on the NACA 23012 aerofoil,” *Experiments in Fluids*, Vol. 9, 1990, pp. 49–58.
13. Mulleners, K. and Raffel, M., “Dynamic Stall Development,” *Experiments in Fluids*, Vol. 54(2), 2013, doi:10.1007/s00348-013-1469-7.
14. Merz, C.B., Wolf, C.C., Richter, K., Kaufmann, K., Mielke, A. and Raffel, M, “Spanwise Differences in Static and Dynamic Stall on a Pitching Rotor Blade Tip Model,” *Journal of the American Helicopter Society*, Vol. 62(1), 2017, doi:10.4050/JAHS.62.012002.
15. Letzgus, J., Kessler, M., and Kraemer, E., “Simulation of Dynamic Stall on an Elastic Rotor in High-Speed Turn Flight,” *Journal of the American Helicopter Society*, Vol. 65(1), 2020, doi: 10.4050/JAHS.65.022002.
16. Weiss, A., Geisler, R., Schwermer, T., Yorita, D., Henne, U., Klein, C., and Raffel, M., “Single-shot pressure-sensitive paint lifetime measurements on fast rotating blades using an optimized double-shutter technique,” *Experiments in Fluids*, Vol. 58(9), 2017.
17. Bauknecht, A., Wang, X., Faust, J-A. and Chopra, I., “Wind Tunnel Test of a Rotorcraft with Lift Compounding,” *Journal of the American Helicopter Society*, Vol. 66, 2021 , doi: 10.4050/JAHS.66.012002.
18. Han, C.H., Yun, C.Y., Kim, S.J. and Jung, S.N., “Aeromechanical Stability Investigation of a Composite Hingeless Rotor in Hover,” *Journal of the American Helicopter Society*, Vol. 48, 2003, <https://doi.org/10.4050/JAHS.48.159>.
19. Lütke, B., Schmidt, M., Sinske, J., and Neumann, J., “Structural design of an instrumented double-swept wind tunnel Model,” *International Conference on Composite Materials*, Copenhagen, 2015.
20. Schwermer, T., Richter, K., and Raffel, M., “Development of a rotor test facility for the investigation of dynamic stall,” *New Results in Numerical and Experimental Fluid Mechanics X, Springer*, Vol. 6(7), 2016, pp. 663–673.
21. Letzgus, J., Gardner, A., Schwermer, T., Kessler, M., and Kraemer, E., “Numerical Investigations of Dynamic Stall on a Rotor with Cyclic Pitch Control,” *Proceedings of the 43rd European Rotorcraft Forum*, 12-15 September, Milan, 2017.
22. Goerttler, A., Braukmann, J., Schwermer, T., Gardner, A., and Raffel, M., “Tip-Vortex investigation on a rotating and pitching rotor blade,” *43th European Rotorcraft Forum*, 12-15 September, Milan, 2017.
23. Schwermer, T., Gardner, A., and Raffel, M., “Dynamic Stall Experiments on a Rotor with High Cyclic Setting in Axial Inflow,” *Proceedings of the 73rd Annual Forum of the American Helicopter Society*, 9-11 Mai, Fort Worth, Texas, 2017.
24. Braukmann, J., Schwermer, T., and Wolf, C., “Investigation of young blade-tip vortices at a rotor test facility using stereoscopic PIV,” *Fachtagung ”Experimentelle Stroemungsmechanik”*, 5-7 September, Karlsruhe, 2017.
25. Müller, M.M., Schwermer, T., Mai, H., and Stieg, C., “Development of an innovative double-swept rotor blade for the rotor test facility Göttingen,” *DLRK 2018 - Deutscher Luft- und Raumfahrtkongress, DGLR - Deutsche Gesellschaft für Luft - und Raumfahrt - Lilienthal-Oberth e.V., Friedrichshafen*, 4-6 September, URL <https://elib.dlr.de/122702/>.
26. Kaufmann, K., Müller, M., and Gradner, A., “Dynamic stall computations of double-swept rotor blades,” In: Dillmann, A., Heller, G., Krämer, E., Wagner, C., Tropea, C., Jakirlic, S. New results in numerical and experimental fluid mechanic XII: contributions to the 21st STAB/DGLR symposium Darmstadt, Germany, 2018, *Notes on Numerical Fluid Mechanics and Multidisciplinary Design*, vol 142, pp. 351–361, <https://doi.org/10.1007/978-3-030-25253-3-34>.
27. Weiss, A., Geisler, R., Müller, M.M., Klein, C., Henne, U., Braukmann, J.N., and Letzgus, J., “Dynamic-stall measurements using time-resolved pressure-sensitive paint on double-swept rotor blades,” *Experiments in Fluids*, Vol. 63(15), 2021, <https://doi.org/10.1007/s00348-021-03366-6>.
28. Skopinski, T. H., Aiken, W. S. Jr., Huston, W. B., “Technical Note: Calibration of strain-gauge installations in aircraft structures for the measurement of flight loads,” *National Advisory Committee for Aeronautics*, 1953.
29. Splettstroesser, W.R., Prieur, J., Pahlke, K., Schultz, K.-J., van der Wall, B.G., Delrieux, Y., Gardarein, P., Geofroy, P., and Leconte, P., “Investigation of young blade-tip vortices at a rotor test facility using stereoscopic PIV,” *DLR Internal Report, DLR-IB 129-97/10*, Braunschweig, 1997.
30. Delrieux, Y., Prieur, J., Costes, M., Gardarein, P., Beaumier, H., des Rochettes, H.M., Leconte, P., Crozier,

- P., Splettstroesser, W.R., van der Wall, B.G., Junker, B., Schultz, K.-J., Mercker, E., Pengel, K., Philippe, J.J., and Gmelin, B., "The ONERA-DLR Aeroacoustic Rotor Optimisation Programme ERATO: Methodology and Achievements," *American Helicopter Society Aerodynamics, Acoustics and Test and Evaluation Technical Specialists Meeting*, San Francisco, 2002.
31. Sugimoto, T., Sugioka, Y., Numata D., Nagai, H., Asai, K., "Characterization of frequency response of pressure-sensitive paints," *AIAA Journal of Aircraft*, Vol.55(4), 2017, pp. 1460–1464, <https://doi.org/10.2514/1.J054985>.
 32. Gößling, J., Ahlefeldt, T., Hilfer, M., "Experimental validation of unsteady pressure-sensitive paint for acoustic applications," *Experimental Thermal and Fluid Science*, 2020, <https://doi.org/10.1016/j.expthermflusci.2019.109915>.
 33. Gregory, J.W., Kumar, P., Peng, D., Fonov, S., Crafton, J., Liu, T., "Integrated optical measurement techniques for investigation of fluidstructure interactions," *AIAA fluid dynamics conference*, 5-9 June, San Antonio, Texas, 2017, <https://doi.org/10.2514/6.2009-4044>.
 34. Juliano, T.J., Kumar, P., Peng, D., Gregory, J.W., Crafton, J., Fonov, S., "Single-shot, lifetime-based pressure-sensitive paint for rotating blades," *Measurement Science and Technology*, vol.22(8):085403, 2011, <https://doi.org/10.1088/0957-0233/22/8/085403>.
 35. Geisler, R., "A fast double shutter system for CCD image sensors," *Measurement Science and Technology*, vol.25(2):025404, 2014, <https://doi.org/10.1088/0957-0233/25/2/025404>.
 36. Geisler, R., "A fast double shutter for CCD-based metrology," In: *Shiraga H, Etoh TG (eds) Selected papers from the 31st international congress on high-speed imaging and photonics*, SPIE, Osaka, vol.10328, p. 1032809, 2017, <https://doi.org/10.1117/12.2269099>.
 37. van der Wall, B. G., "Grundlagen der Hubschrauber-Aerodynamik," *Springer, Heidelberger Platz 3, Berlin*, 2015.
 38. van der Wall, B. G., "Grundlagen der Dynamik von Hubschrauber-Rotoren," *Springer, Heidelberger Platz 3, Berlin*, 2018.